

# Orders of magnitude runtime reduction in quantum error mitigation

Raam Uzdin

*Fritz Haber Research Center for Molecular Dynamics, Institute of Chemistry,  
The Hebrew University of Jerusalem, Jerusalem 9190401, Israel*

Quantum error mitigation (QEM) infers noiseless expectation values by combining outcomes from intentionally modified, noisy variants of a target quantum circuit. Unlike quantum error correction, QEM requires no additional hardware resources and is therefore routinely employed in experiments on contemporary quantum processors. A central limitation of QEM is its substantial sampling overhead, which necessitates long execution times where device noise may drift, potentially compromising the reliability of standard mitigation protocols. QEM strategies based on agnostic noise amplification (ANA) are intrinsically resilient to such noise variations, but their sampling cost remains a major practical bottleneck. Here we introduce a mitigation framework that combines virtual noise scaling with a layered mitigation architecture, yielding orders of magnitude reduction in runtime overhead compared to conventional zero-noise extrapolation post-processing. The proposed approach is compatible with dynamic circuits and can be seamlessly integrated with error detection and quantum error correction schemes. In addition, it naturally extends to ANA-based mitigation of mid-circuit measurements and preparation errors. We validate our post-processing approach by applying it to previously reported experimental data, where we observe a substantial improvement in mitigation efficiency and accuracy.

Even after error correction is successfully implemented, quantum computers will not be noise-free, as quantum error correction schemes (QEC) struggle with correlated errors, leakage errors, and other non-idealities. An emerging strategy [1–7] is to complement QEC with quantum error mitigation (QEM) protocols [8–41] which are already widely used for handling errors in the pre-fault-tolerant era [19, 28, 30–35, 42–44]. QEM methods remove the noise bias from the expectation values at the cost of increasing the variance, thereby increasing the sampling cost. To counter this increase, more shots have to be executed and the runtime increases accordingly. Crucially, unlike QEC, QEM involves little or no hardware overhead.

The two most widely used schemes are probabilistic error cancellation (PEC) and agnostic noise amplification (ANA). In PEC and its variants [11, 22, 45], noise characterization and a simplified sparse noise model are required for removing the noise from expectation values. As such, these methods are vulnerable to noise drifts in which the noise parameters change during the execution of the experiment. As a result, the learned noise model no longer represents the actual noise and residual noise appears. ANA, on the other hand, does not involve characterization. In this approach, the noise is amplified by a known factor by constructing special noisy variants of the target circuit. The ANA approach has two key advantages (1) it can mitigate non-sparse noise models which are very difficult to address in PEC, (2) it can be made fully resilient to temporal drifts of the noise parameters, i.e. handle non-stationary noise. Note that the widely used zero noise extrapolation (ZNE) is not necessarily noise agnostic. ZNE is a post-processing technique that uses measurement with multiple noise amplification factors to predict the noiseless expectation values but the noise amplification can be done either in an agnostic manner or using characterization as done in probabilistic error amplification (PEA) [43]. We point out that a class of methods called virtual purification [19, 40, 46] is also agnostic but it is applicable only to special types of noise. Furthermore, the purification approach involves hardware overhead.

To experimentally implement ANA, various techniques have been proposed, including (i) pulse stretching [11, 47] (ii) digital local folding, also known as gate insertion, and digital global folding [48–50], and (iii) the pulse-inverse KIK [51] method and its refined and enhanced version “Layered KIK” [52]. Pulse stretching is challenging to implement and calibrate and is also inconsistent with twirling techniques [53–56] for treating coherent errors. Digital folding has been shown analytically and experimentally to be incorrect even at the leading order of the noise, leading to results which significantly deviate from the ideal value (regardless of the sampling overhead invested).

In this work we start by studying the fidelity limit of the Taylor-based post-processing and introduce a method for reducing the runtime overhead by orders of magnitude when the noise is strong.

## I. PRELIMINARIES

### A. Noise amplification in Liouville space

In this work we describe the quantum state of the system using density vectors  $|\rho\rangle$  in Liouville space [57]. The vector  $|\rho\rangle$  is obtained by flattening the density matrix into a column vector. In this representation, quantum channels

act linearly from the left on the state, which makes it convenient for describing noisy quantum dynamics.

If the ideal evolution in Hilbert space is given by a unitary operator  $U_H$ , then the corresponding ideal evolution in Liouville space is  $U = U_H \otimes U_H^*$ . The noisy evolution operator can be written as

$$K = UN. \quad (1)$$

where  $N$  is the noise channel operator in Liouville space. Noise amplification by a factor  $\alpha$  is defined as

$$K_{amp} = UN^\alpha. \quad (2)$$

In this work we focus on odd amplification powers. Excluding pulse stretching, all agnostic noise amplification (ANA) methods naturally lead to odd amplification factors. This originates from the use of a circuit (or gate) together with its inverse in order to amplify the noise. As shown in [52], if the evolution operator is sliced into layers  $K = K_1 \dots K_L$  then, when the number of layers is sufficiently large, the following relation holds:

$$UN^{2j+1} \cong K_1(K_1^I K_1)^j \dots K_L(K_L^I K_L)^j, \quad (3)$$

where  $K_\ell^I$  denotes the pulse inverse of layer  $\ell$ . Throughout this work, the symbol  $\cong$  is used to denote equality for all practical purposes, meaning that the approximation becomes arbitrarily accurate when a sufficiently large number of layers is used. We therefore assume that, for practical implementations, perfect noise amplification can be achieved.

Finally, we note that even if the native noise generators, that is, the Lindbladians, are Hermitian, the effective noise channel  $N$  is generally not Hermitian due to time ordering. In a Magnus expansion,  $N = e^{\sum_k \Omega_k}$ , the leading term  $\Omega_1$  is Hermitian when the Lindbladians are Hermitian, whereas the second-order term  $\Omega_2$  is anti-Hermitian. Noise Hermiticity plays an important role in the present work. In the next section, we show how Hermiticity can be effectively restored, even when the given noise channel is not Hermitian.

## B. Taylor-based mitigation

Using  $K = UN$  for the noisy circuit evolution operator, the Taylor-based  $m$ -th order mitigated evolution operator is [51]

$$K_{mit}^{(m)} \cong \sum_{k=0}^m a_{j,Tay}^{(m)} UN^{2j+1}, \quad (4)$$

$$a_{j,Tay}^{(m)} = \frac{(-1)^j (2m+1)!!}{2^m (2j+1) j! (m-j)!}. \quad (5)$$

The Taylor coefficients  $a_{j,Tay}^{(m)}$  coincide with the Richardson extrapolation coefficients [2, 20] used in zero-noise extrapolation (ZNE) when odd noise-amplification factors are employed [51]. In the limit  $m \rightarrow \infty$ , one obtains  $K_{mit}^{(m)} \rightarrow U$ , indicating that the Taylor coefficients are bias-free (asymptotically). This result follows directly from the KIK formula presented in [51] and is also consistent with the finite-order fidelity analysis developed in the present work.

### 1. $\frac{1}{\sqrt{x}}$ Taylor expansion picture

It was shown in [51] that even when the noise is not Hermitian, the following relation holds

$$U = K \frac{1}{\sqrt{K_I K}} + O(\Omega_2). \quad (6)$$

This relation, referred to as the *KIK formula*, correctly captures the small bias arising from the residual second-order Magnus term  $\Omega_2$ . The formula was later extended to layer-based noise amplification schemes (“local-folding”). In this framework, the Taylor coefficients arise from expanding the function  $(K_I K)^{-1/2}$  around the point  $K_I K = I$ , corresponding to the zero-noise limit. This provides a rigorous alternative interpretation of the commonly used zero-noise extrapolation post-processing. From this perspective, error mitigation reduces to approximating the function  $1/\sqrt{x}$  by a power series in  $x$ . When the noise is Hermitian (see Sec. I B 4), the spectrum satisfies  $x \in (0, 1]$ . In practice, however, the noise spectrum occupies only a subinterval of this range. This observation allows one to choose a power-series approximation that is optimized over the effective noise interval, rather than using the Taylor

coefficients, which are optimized at  $x = 1$ . In [51] it was demonstrated that optimizing over this relevant interval outperforms the Taylor-based mitigation using the same experimental data.

In [51], the effective noise interval was estimated using an additional echo measurement. In the present work, we introduce an alternative approach with three key features: (i) it does not require additional measurements to estimate the noise, (ii) it is automatically optimized for the specific observable of interest, and (iii) it is compatible with mid-circuit measurements. The performance and runtime cost of this approach are analyzed in the remainder of the paper.

## 2. Drift resilience

As shown numerically in Supplementary note 3 of [51] and analytically in the end of Appendix I of [52], Taylor-based mitigation is drift resilient provided that agnostic noise amplification is available and the circuit execution order is chosen correctly. All noise-amplified circuits must be executed for a small number of shots during which the noise can be assumed to be stable. This set of executions is then repeated many times to reach the desired statistical accuracy. In the extreme case, each set contains a single shot from each circuit.

## 3. Bias-free

Since  $K_I K \cong N^2$ , the KIK formula yields

$$K_{mit}^{(\infty)} = K \frac{1}{\sqrt{K_I K}} \cong UN \frac{1}{\sqrt{N^2}} = U. \quad (7)$$

$K_{mit}^{(\infty)}$  represents infinite order Taylor mitigation. As shown in [52], the small  $O(\Omega_2)$  correction implied by the  $\cong$  sign can be strongly suppressed by layer-wise amplification. Consequently, the Layered-KIK formula is bias-free for all practical purposes.

## 4. Hermiticity of the effective noise

As explained in [52] and in Appendix VI of the present paper, even if the native noise is Hermitian (e.g. due to decoherence or Pauli errors), the effective noise channel of the circuit  $N$  is generally not Hermitian due to time ordering. The leading contribution to this non-Hermiticity is given by the second-order Magnus term  $\Omega_2$  of  $N$ . As shown in [52] when noise amplification is performed in layers,  $\Omega_2$  for the full circuit has two contributions: (i) the  $\Omega_2$  term of each individual layer, and (ii) cross terms arising from commutators of the first-order terms  $\Omega_1$  from different layers.

The first contribution becomes negligible when the number of layers is sufficiently large (on the order ten). Importantly, this does not introduce any additional runtime penalty or sampling overhead compared to single-layer mitigation. The second contribution is eliminated when Taylor mitigation of order two or higher is applied. Therefore, when using a sufficiently large number of layers and mitigation order  $M \geq 2$ , the  $\Omega_2$  term can be neglected. As a result, the leading source of non-Hermiticity is canceled when using Layered KIK, and the effective noise satisfies  $N_{\text{eff}} = N_{\text{eff}}^\dagger$ . For brevity, we drop the subscript “eff” in the remainder of the paper.

Since the noise is Hermitian, it admits a spectral decomposition in Liouville space,

$$N = \sum s_i |s_i\rangle \langle s_i|, \quad (8)$$

where  $0 < s_i \leq 1$ .  $s_i \rightarrow 0$  corresponds to infinite noise, while  $s_i \rightarrow 1$  corresponds to zero noise. In this work we assume the native noise is Hermitian, since it is possible to apply pseudo-twirling [56] in sufficiently thin layers to render the noise in each layer Hermitian.

## II. INFIDELITY AND ITS COST AT FINITE MITIGATION ORDER

Using standard properties of the operator norm  $\|A\|_{op} = \sqrt{\max[\text{eig}(A^\dagger A)]}$  we get

$$|\langle A \rangle_{\text{ideal}} - \langle A \rangle_{\text{mit}}^{(m)}| \leq \|U - K_{\text{mit}}^{(m)}\| \sqrt{\text{tr} \bar{A}^2} \sqrt{\text{tr} \rho_0^2}, \quad (9)$$

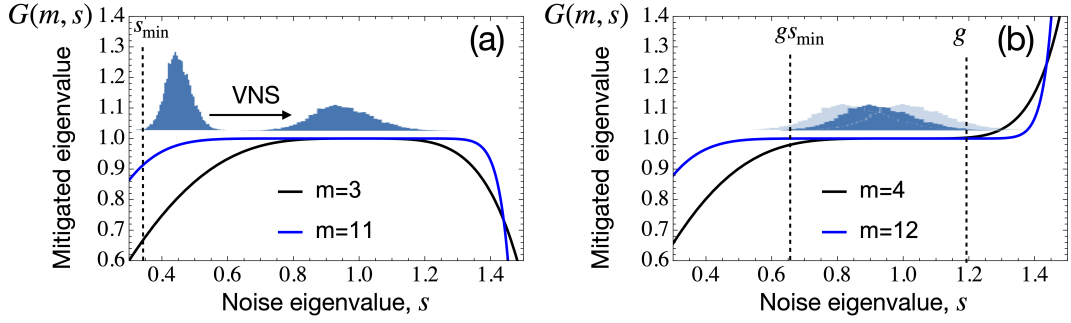


Figure 1. Plots of the mitigation function  $G(m, s)$  for odd (a) and even (b) orders. As the order increases, the plateaus become wider, and a broader range of noise eigenvalues is mapped to 1, corresponding to successful mitigation. The left histogram in (a) represents the noise histogram of the circuit. By applying our VNS method, the histogram is shifted to the center of the plateau (right histogram), where the mitigation performance is significantly improved. The histograms in (b) illustrate that when the scaled noise interval  $[gs_{\min}, g]$  is narrower than the width of the plateau, small changes in  $g$  do not affect the value of the mitigated observable. We exploit this principle to determine  $g$  from the noise-amplified expectation value.

where  $\bar{A}$  denotes the observable  $A$  with its trace removed. Using unitary invariance of the operator norm and assuming Hermitian noise, this bound can be written as

$$\left\| U - K_{\text{mit}}^{(m)} \right\|_{\text{op}} = \left\| I - U^\dagger K_{\text{mit}}^{(m)} \right\|_{\text{op}} = \max_i |1 - \sum_{k=0}^m a_k^{(m)} s_i^{2k+1}|. \quad (10)$$

Interestingly, the sum appearing above can be expressed in closed form as

$$G(m, s_i) = \sum_{k=0}^m a_{k, \text{Tay}}^{(m)} s_i^{2k+1} = s_i \frac{{}_2F_1(3/2, -m, 1/2, s_i^2)}{{}_2F_1(3/2, -m, 1/2, 1)}, \quad (11)$$

where  ${}_2F_1$  is the Gauss hypergeometric function and  ${}_2F_1(3/2, -m, 1/2, 1) = \frac{2^{-m}(2m+1)!!}{m!}$ . For convenience, we define  $F(-m, x) = {}_2F_1(3/2, -m, 1/2, x)$ .  $G$  is the *mitigation function* and it describes to what extent the noise eigenvalues are mapped to 1 which corresponds to zero noise. As shown in Fig. 1, larger mitigation orders lead to broader “plateaus” where the input noise eigenvalues are mapped to one with high accuracy. Previous studies deal with the regime  $s \leq 1$  that contain the physical noise histogram (left histogram in Fig. 1 (a)). In this work we exploit the fact that the plateaus extend into the  $s > 1$  regime. Our virtual noise scaling (VNS) technique improves the mitigation performance by shifting the noise histogram to the center of the plateau (right histogram in Fig. 1 (a)).

Since  $G(m, s)$  is monotonically increasing in  $s$  for any positive integer  $m$  and  $0 < s < 1$ , the operator norm is determined by the smallest singular value  $s_{\min}$  and becomes

$$\left\| U - K_{\text{mit}}^{(m)} \right\|_{\text{op}} = \left| 1 - \sum_{k=0}^m a_{k, \text{Tay}}^{(m)} s_{\min}^{2k+1} \right| = 1 - G(m, s_{\min}) = 1 - \frac{s \int_0^{s_{\min}} (1-t^2)^m dt}{\int_0^1 (1-t^2)^m dt} \triangleq I_{\text{op}}^{(m)}(s_{\min}), \quad (12)$$

where we have used monotonicity and the fact that  $\frac{sF(-m, s^2)}{F(-m, 1)}|_{s=1} = 1$  to remove the absolute value. The quantity  $I_{\text{op}}^{(m)}(s_{\min})$  defines the infidelity function and together with (9) it quantifies the worst-case error in estimating noiseless expectation values using  $m$ -th order Taylor mitigation.

In this work we study the relations between the unmitigated infidelity, the mitigated fidelity and the runtime overhead (sampling overhead and depth overhead). The sampling overhead  $\gamma_m^2 = (\sum_{k=0}^m |a_k^{(m)}|)^2$  can also be expressed in terms of the Gauss hypergeometric function

$$\gamma_m = \frac{F(-m, -1)}{F(-m, 1)} = \frac{\int_0^1 (1+t^2)^m dt}{\int_0^1 (1-t^2)^m dt}. \quad (13)$$

While  $\gamma_m^2$  captures the sampling overhead, the total runtime overhead  $\mathcal{R}$  must also account for the increased circuit depth associated with noise amplification. An amplification factor  $2j + 1$  increases the circuit depth by the same

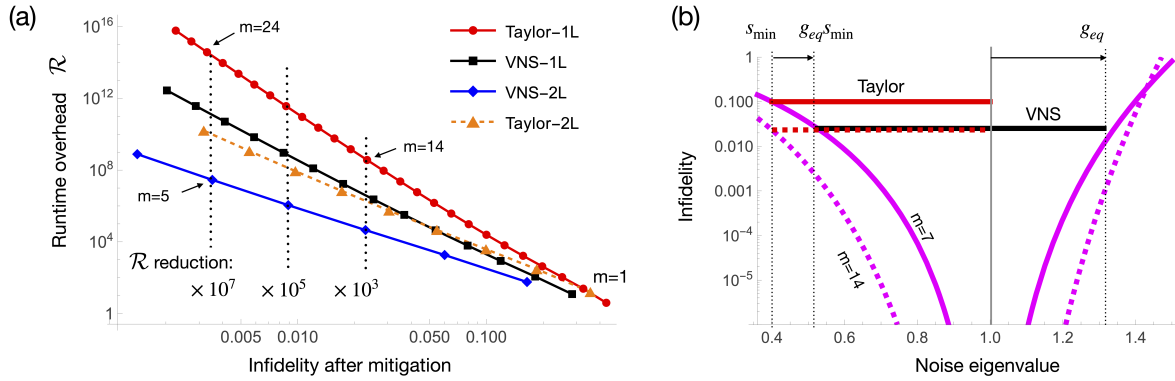


Figure 2. (a) The red curve shows the runtime overhead  $\mathcal{R}$  of standard Taylor mitigation as a function of the mitigated worst-case infidelity with the markers indicating the mitigation order  $m$ . The black curve, shows that the virtual noise scaling (VNS) introduced in the present work, leads to a substantial reduction of the runtime overhead. The initial infidelity is 0.6 which corresponds to strong noise. To achieve an even larger reduction in  $\mathcal{R}$ , we combine VNS with a two-layer mitigation protocol (blue curve). The corresponding runtime overhead reduction factors for several target infidelities are indicated below the vertical dotted lines. This orders-of-magnitude reduction in  $\mathcal{R}$  can make previously unrealistic mitigation performance feasible. For reference, the orange curve shows two-layer mitigation without VNS. (b) The solid purple funnel shows the mitigated infidelity as a function of the noise eigenvalue for mitigation order seven ( $m = 7$ ). The smallest eigenvalue,  $s_{\min} = 0.4$ , determines the worst-case infidelity. After applying VNS, the original noise interval (red) is mapped to the black interval. Although this interval is wider, the new extreme point  $g_{eq}s_{\min}$  corresponds to a smaller infidelity. For comparison, the dashed purple funnel shows the infidelity for mitigation order  $m = 14$ , which is the order required to achieve the same infidelity as the  $m = 7$  mitigation with VNS.

factor,  $d = 2j + 1$ . When this effect is included, the runtime overhead is

$$\mathcal{R} = \gamma_m^2 \langle d \rangle, \quad (14)$$

where  $\langle d \rangle$  is the averaged depth increase. For  $m \geq 3$  Taylor mitigation, we find in Appendix VI that  $\langle d \rangle \simeq m$ . The runtime overhead grows exponentially with circuit size, since larger mitigation orders are required to reach a fixed target infidelity. Consequently, QEM is not a pathway to scalability. Rather, it is a method for obtaining high-fidelity results from devices whose noise is significant but not extreme. We refer to this regime of QEM applicability as *benign noise*, defined by  $I_{\text{op}}^{(0)} = 1 - s_{\min} \leq 1/2$ . This is not a strict definition, and stronger noise can be mitigated at a higher cost. As hardware improves and QEC becomes practical, the circuit sizes that fall within the benign-noise regime after QEC will increase.

Although  $\mathcal{R}$  grows exponentially with  $m$ , the infidelity  $I_{\text{op}}^{(m)}$  decays approximately exponentially with  $m$ . In fact,  $\mathcal{R}$  and  $I_{\text{op}}$  are related by an approximate power law. Consequently,  $\mathcal{R}(I_{\text{op}})$  appears approximately linear on a log-log scale. This behavior is illustrated by the red curve in Fig. 2. The initial fidelity in that example is  $I_{\text{op}}^{(0)} = 0.6$ .

The trade-off between exponential error suppression and exponential sampling overhead is particularly transparent in the large- $m$  limit,

$$I_{\text{op}}^{(m)}(s_{\min}) \xrightarrow{m \gg 1} \frac{(1 - s_{\min}^2)^{m+1}}{\sqrt{\pi m} s_{\min}}, \quad (15)$$

$$\gamma_m^2 \xrightarrow{m \gg 1} \frac{4^{m+1}}{\pi m}. \quad (16)$$

For a given initial infidelity  $1 - s_{\min}$  the linear slope  $a = \frac{d \log(\gamma_m^2 m)}{d \log I_{\text{op}}^{(m)}(s_{\min})}$  in the log-log implies  $\log(\gamma_m^2 m) = a \log I_{\text{op}}^{(m)}(s_{\min}) + b$  or equivalently  $\gamma_m^2 m = e^b (I_{\text{op}}^{(m)}(s_{\min}))^a$ , i.e., a power law. The often-stated exponential overhead with circuit size is encapsulated in the value of  $s_{\min}$ . However, for a fixed circuit, the cost of further reducing the mitigated infidelity follows a power-law scaling.

### III. VNS - VIRTUAL NOISE SCALING

The standard Taylor mitigation scheme is based on an expansion around the point  $s = 1$ . However, since  $0 < s \leq 1$ , this expansion point is generally not centered within the eigenvalue distribution of the noise, and the resulting approximation is suboptimal. We therefore propose to rescale all occurrences of the noise operator  $N$  by a constant factor  $g$ , that is,  $K \rightarrow K_g = gK$  and  $K_I \rightarrow K_{I,g} = gK_I$ . As a result, the mitigated evolution operator becomes

$$K_{mit}^{(m)}(g) = \sum_{k=0}^m a_k^{(m)}(g) K (K_I K)^k \cong U \sum_{k=0}^m a_k^{(m)}(g) N^{2k+1}, \quad (17)$$

with rescaled coefficients

$$a_k^{(m)}(g) = a_{k,Tay}^{(m)} g^{2k+1}. \quad (18)$$

Since the eigenvalues of  $gN$  are simply  $gs_i$ , one may choose  $g > 1$  so that the eigenvalue distribution is shifted closer to the expansion point  $s = 1$ . Several choices for the scaling factor  $g$  are possible, for example,

$$g = 1/\sqrt{s_{\min}}, \quad g = 2/(1 + s_{\min}), \quad g_{eq} = \sqrt{\frac{2}{s_{\min}^2 + 1}} \quad \text{and} \quad g_{det} = 1/\det(N)^{1/n^2} \quad \text{where } n \text{ is the Hilbert space dimension.}$$

The choice  $g = g_{det}$  is equivalent to removing the trace component of the first Magnus term  $\Omega_1$ , since  $N \cong e^{\Omega_1}$ . Other choices do not remove the trace but approximately center  $\Omega_1$  around zero. While we choose a specific function  $g(s_{\min})$  in order to study the potential of this approach, we later present a simple procedure for determining  $g$  directly from the measured, noise-amplified expectation values.

After rescaling by  $g$ , the spectrum of  $gN$  lies in the interval  $[gs_{\min}, g]$ . The corresponding infidelity is therefore

$$\left\| I - U^\dagger K_{mit}^{(m)}(g) \right\|_{op} = \max[I_{op}^{(m)}(gs_{\min}), |I_{op}^{(m)}(g)|] \triangleq I_{op}^{(m)}(s_{\min}, g). \quad (19)$$

Virtual noise scaling also affects  $\gamma_m$ , which becomes

$$\gamma_m(g) = \sum_{k=0}^m \left| a_k^{(m)}(g) \right| = \frac{gF(-m, -g^2)}{F(-m, 1)} \quad (20)$$

In the weak-noise limit  $s_{\min} \rightarrow 1$ , one finds that for  $m \geq 1$  the infidelity reduction is exponential, while at the same time there is no additional sampling overhead,

$$\lim_{s_{\min} \rightarrow 1} \frac{I_{op}^{(m)}(s_{\min}, g_{eq})}{I_{op}^{(m)}(s_{\min}, g)} = 2^{m+1}, \quad (21)$$

$$\lim_{s_{\min} \rightarrow 1} \frac{\gamma_m(g_{eq})}{\gamma_m(1)} = 1. \quad (22)$$

However, for  $m \gtrsim 5$  the infidelity is already below typical experimental accuracy, and it is therefore not clear that the additional mitigation power is required. While the advantage of virtual noise scaling is clear in the strong-noise regime, the associated increase in runtime overhead cannot be ignored. This motivates a direct comparison between virtual noise scaling and standard Taylor mitigation at different orders. In particular, one should compare mitigation orders  $m$  and  $m_{VNS}$  that yield the same infidelity. Although virtual noise scaling at a given order  $m$  is always associated with an increased  $\mathcal{R}$ , it is possible that a lower-order VNS protocol outperforms an  $m$ th-order Taylor mitigation scheme. This behavior is illustrated in Fig. 2 (a). The red curve shows the runtime overhead  $\mathcal{R}$  of Taylor mitigation as a function of the infidelity for  $s_{\min} = 0.4$ . The vertical dotted line indicates that, for the same infidelity, a lower-order VNS protocol achieves a smaller runtime overhead. In this simulation, we used  $g = \sqrt{\frac{2}{1+s_{\min}^2}}$ .

In the large- $m$  limit, the VNS infidelity and  $\mathcal{R}$  scale as

$$I_{op, VNS-1L}^{(m)} \xrightarrow{m \gg 1} \frac{(1 - g_{eq}^2 s_{\min}^2)^{m+1}}{\sqrt{\pi m} g_{eq} s_{\min}}, \quad (23)$$

$$\gamma_m^2 m \xrightarrow{m \gg 1} \frac{(1 + g_{eq}^2)^{2m+2}}{\pi g_{eq}^2}. \quad (24)$$

Here we used the fact that, for  $g = g_{eq}$ ,  $\max(I_{op}^{(m)}(g_{eq}s_{\min}), |I_{op}^{(m)}(g_{eq})|) = I_{op}^{(m)}(g_{eq}s_{\min})$ . For a fixed mitigation order, the infidelity is therefore suppressed by a factor  $(1/(1 + s_{\min}^2))^{m+1}$ . The VNS advantage can be visualized more

clearly using the infidelity funnels depicted in 2(b). While the VNS improvement is substantial, achieving orders-of-magnitude reductions in runtime overhead when the noise is strong requires combining virtual noise scaling with mitigation in layers, as discussed in Sec. IV. Before doing so, we present a methodology for determining the scaling factor  $g$  without prior knowledge of the noise and without additional experimental overhead.

### A. Determining the virtual noise scaling factor from the measured expectation values

While noise-scaling formulas such as  $g_{\text{eq}}$  or  $\bar{g}$  (see Appendix VI) can be useful, they require prior knowledge of  $s_{\min}$ . As shown in Appendix VI,  $s_{\min}$  can be lower bounded by the infidelity contributions of the individual gates in the circuit. Assuming local noise, and that each “gate”  $i$  is associated with a parameter  $s_{\min,i}$ , we find  $s_{\min}^{\text{circuit}} \geq \prod_i s_{\min,i}$ .

Importantly, the term “gate” refers to any time interval during which noise acts. This definition therefore also includes identity operations on temporarily idle qubits that are subject to noise. If error correction or error mitigation has been applied prior to our protocol,  $s_{\min,i}$  refers to the smallest eigenvalue after that operation. In such cases, the product  $\prod_i s_{\min,i}$  can remain in the benign regime even for large circuits.

Beyond the possibility of overestimating the noise (that is, underestimating  $s_{\min}$ ), such bounds do not account for the dependence on the initial state and the observable of interest. Some initial states or observables may be insensitive to certain noise mechanisms that are present in the circuit. As a result, the effective smallest eigenvalue of the noise, denoted  $s_{\min}^{\text{eff}}$ , can be larger than the smallest eigenvalue of the full noise channel. Restricting attention to noise sources that lie within the effective light cone of the observable, as done for example in light-cone estimation methods [43, 58], can significantly reduce the sampling overhead.

To address this issue, we propose the following simple procedure. First, one plots the mitigated expectation value of an observable  $A$  as a function of  $g$

$$\langle A \rangle_{\text{mit}}^{(m)}(g) = \sum_{k=0}^m a_k^{(m)} g^{2k+1} \langle A \rangle_{2k+1}, \quad (25)$$

where  $\langle A | K(K_I K)^k | \rho_0 \rangle$  is the noise amplified expectation value of interest. Due to the structure of the infidelity function  $G(m, s)$ , choosing  $g$  that is too large or too small (below one) leads to substantial changes in  $\langle A \rangle_{\text{mit}}^{(m)}(g)$ . However, for sufficiently large mitigation order  $m$ , there exists a “plateau regime” in which the infidelity lies below the target accuracy, as illustrated in Fig. 1. If this plateau is wider than the effective noise width  $1 - s_{\min}^{\text{eff}}$ , then the scaled noise interval  $\{gs_{\min}^{\text{eff}}, g\}$  remains inside the plateau (see the histogram illustrations in 1), and  $\langle A \rangle_{\text{mit}}^{(m)}(g)$  becomes largely insensitive to small variations in  $g$  (see piles illustration in 1 (b)). This is also illustrated in the infidelity plots in Fig. 2(b).

The value of  $g$  can therefore be estimated directly from the curve  $\langle A \rangle_{\text{mit}}^{(m)}(g)$  by identifying the range over which the plateau persists. When the mitigation order is large and the plateau is wide compared to the effective noise, one may choose the smallest value  $g > 1$  for which the deviation from the plateau center remains within the target accuracy. Since the sampling overhead increases monotonically with  $g$ , this choice minimizes the runtime overhead.

When the mitigation order is too low to exhibit a clear plateau, we instead search for the closest substitute: either an extremum or, if no extremum exists in the interval  $[1, g_{\max}]$ , an inflection point. For large  $m$ , it is sufficient to take  $g_{\max} = \sqrt{2}$ , since  $G(m, g)$  increases rapidly beyond this value (see Fig. 1). For low mitigation orders ( $m \sim 4$  and below), extrema or inflection points may appear at values of  $g$  larger than  $\sqrt{2}$ . Since  $G(m, s)$  has an extremum for odd orders and an inflection point for even orders (see Fig. 1),  $\langle A \rangle_{\text{mit}}^{(m)}(g)$  often follows the same form. However, since expectation values involve linear combinations of noise modes  $\{s_i\}$ , an extremum may appear before the inflection point.

Although more sophisticated algorithms could yield improved accuracy, we adopt the following simple rule: we first search for an extremum in the interval  $[1, g_{\max}]$ , and if none is found, we search for an inflection point. If neither exists, then either the mitigation order is too low, in which case such features appear only at higher order, or the mitigation order is sufficiently high that standard Taylor mitigation already suppresses the noise below the experimental accuracy. These two cases are easily distinguished. In the former,  $\langle A \rangle_{\text{mit}}^{(m)}(g)$  varies significantly with  $g$ , whereas in the latter a plateau is already present starting at  $g = 1$ , so we simply choose  $g = 1$  to minimize the sampling overhead.

Importantly, the function  $\langle A \rangle_{\text{mit}}^{(m)}(g)$  encodes information about both the observable and the initial state. To illustrate this point, we consider an Ising-like Trotter evolution with local decoherence noise. Figure 3(a) shows the mitigated expectation value of  $\sigma_z$  on the left-end qubit for mitigation orders  $m = 2, 4$ , and  $6$ . The vertical axis shows the deviation from the ideal value, and the horizontal axis shows the VNS parameter  $g$ . As expected from

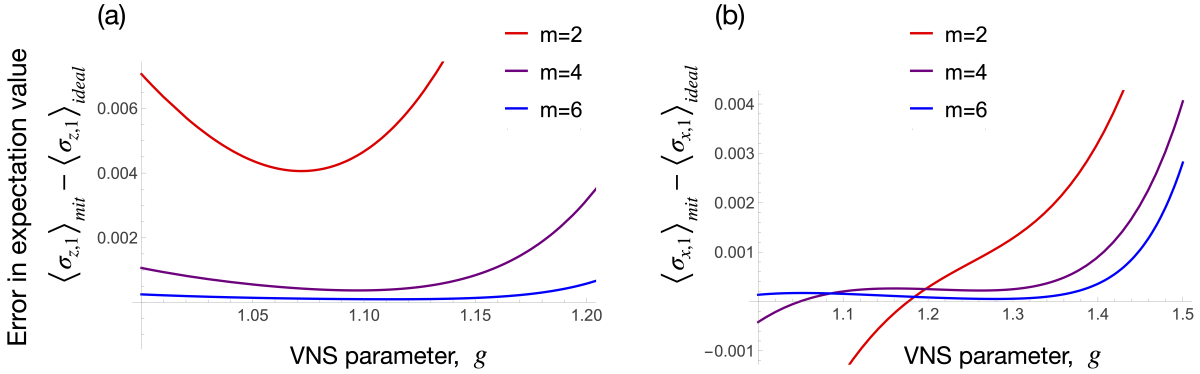


Figure 3. (a) The value of  $g$  can be extracted from the mitigated expectation value as a function of the VNS parameter  $g$ . As the mitigation order  $m$  increases, a broader plateau develops. The value of  $g$  is then chosen as the extremum or the inflection point within this plateau. The numerical simulation is based on a four-qubit Ising Trotterized evolution; see main text for simulation details. In (a), the observable is  $\sigma_z$  of the left qubit, whereas in (b) it is  $\sigma_x$  of the same qubit. While in (a) the optimal value is  $g \simeq 1.1$ , in (b) it is  $g \simeq 1.28$ . This difference reflects the fact that the  $\sigma_z$  observable is less affected by noise (and therefore requires a smaller value of  $g$ ) and can consequently be mitigated with a lower runtime overhead.

the discussion above, the plateau becomes wider as the mitigation order increases, while the error at the base of the plateau decreases.

Figure 3(b) shows the mitigated expectation value of  $\sigma_x$  on the same qubit. The initial state and the evolution are identical to those in Fig. 3(a), yet the optimal scaling parameter is  $g \simeq 1.27$ , compared with  $g \simeq 1.1$  in Fig. 3(a). This highlights a key advantage of the present approach: the value of  $g$  is not determined by a worst-case noise estimate, but by the effective manifestation of the noise on the observable of interest. In this case,  $\sigma_z$  is less affected by the noise and therefore exhibits a smaller optimal  $g$ , which in turn implies a lower runtime overhead for its mitigation.

This four-qubit simulation contains twenty Trotter evolution steps. Each step consists of three layers. In the first layer,  $R_{zz}(1/30)$  rotations are applied to qubit pairs 1–2 and 3–4. In the second layer, all qubits undergo an  $R_x(1/15)$  rotation. Finally, in the third layer, qubits 2 and 3 undergo an  $R_{zz}(1/30)$  rotation. Local decoherence is applied independently to each qubit. In the first and third layers, the coefficient of the  $\sigma_z$  Lindbladians is 1/200. During the second layer, the corresponding decay coefficient is 1/2000.

## B. Explicit form for the first two orders

For first-order mitigation, no inflection point can occur for  $g \neq 0$ . Instead, an extremum appears at  $g_{extr}^{(1)} = \sqrt{\frac{\langle A \rangle_1}{\langle A \rangle_3}}$  and the corresponding mitigated value is

$$\langle A \rangle_{mit}^{(1)} = \sqrt{\frac{\langle A \rangle_1^3}{\langle A \rangle_3}}. \quad (26)$$

This expression is identical to exponential extrapolation with noise scale factors one and three. This formula should not be used when  $\langle A \rangle_3 > \langle A \rangle_1$  or when  $\langle A \rangle_1 \langle A \rangle_3 < 0$ , as it then yields  $g < 1$  or an imaginary value of  $g$ . Such situations may occur when the ideal expectation value is close to zero and circuit noise changes the sign of the measured expectation values. We propose a simple strategy to address this issue. First, choose another observable  $B$  whose expectation value is not close to zero within the experimental accuracy, that is, an observable that differs from zero by several standard deviations. Next, compute the mitigated value of  $\langle A \rangle$  using

$$\langle A \rangle_{mit} = \langle A + B \rangle_{mit} - \langle B \rangle_{mit}, \quad (27)$$

where Eq. (26) is separately applied to  $A + B$  and  $B$ . At first order, the effective noise channel may not be Hermitian, in contrast to the assumption used in higher-order analysis.

For second-order mitigation with virtual noise scaling, an inflection point occurs at  $g_{infl}^{(2)} = \sqrt{\frac{\langle A \rangle_3}{\langle A \rangle_5}}$  and the resulting

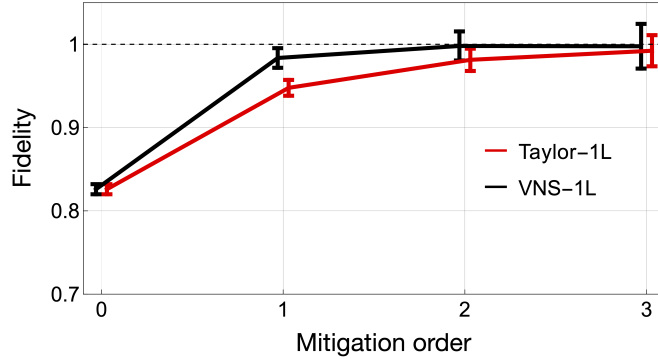


Figure 4. The red curve shows the fidelity of a GHZ state creation experiment reported in [59]. The GHZ state is created using a dynamic circuit. The mid-circuit measurements, mid-circuit resets, and final measurements are simultaneously mitigated using the parity mitigation method, which is resilient to noise drifts. The black curve shows an improvement over the Taylor post-processing when applying VNS to the same experimental data.

mitigated value is

$$\langle A \rangle_{mit}^{(2,infl)} = \frac{15}{8} \sqrt{\frac{\langle A \rangle_3}{\langle A \rangle_5}} \langle A \rangle_1 - \frac{7}{8} \sqrt{\frac{\langle A \rangle_3^5}{\langle A \rangle_5^3}}. \quad (28)$$

As in the first-order case, if  $g_{\text{infl}}^{(2)}$  is imaginary, this indicates a noise-induced sign change of the observable, and the same strategy described above should be used to address this issue.

### C. Virtual noise scaling in dynamic circuits and measurement error mitigation

In [52] it was shown that amplifying the noise in layers using the pulse-inverse KIK method leads to two main advantages: (i) suppression of higher-order Magnus terms to the point where their residual contribution is negligible for all practical purposes, and (ii) applicability to dynamic circuits that include mid-circuit measurements and feedforward. However, the coefficients used in [52] are still the standard Taylor coefficients. The efficient adaptive coefficients introduced in [51] rely on knowledge of the effective noise interval, which is obtained from an echo experiment. However, this simple echo scheme is incompatible with dynamic circuits, since the echo is affected not only by gate noise but also by mid-circuit measurements.

Virtual noise scaling does not suffer from this limitation. VNS can be interpreted as a layer-dependent shifts of the first Magnus term  $\Omega_1$  in each layer, which together represent the noise of the entire circuit, i.e.,

$$\begin{aligned} gUN &= g_1 U_1 e^{\Omega_1^{(1)}} \dots g_l U_l e^{\Omega_1^{(l)}} \dots g_L U_L e^{\Omega_1^{(L)}} \\ &= U_1 e^{(\Omega_1^{(1)} + \ln g_1 I)} \dots U_l e^{(\Omega_1^{(l)} + \ln g_l I)} \dots U_L e^{(\Omega_1^{(L)} + \ln g_L I)}, \end{aligned} \quad (29)$$

and in the same way

$$g^{2j+1}UN^{2j+1} = U_1 e^{(2j+1)(\Omega_1^{(1)} + \ln g_1 I)} \dots g_l U_l e^{(2j+1)(\Omega_1^{(l)} + \ln g_l I)} \dots g_L U_L e^{(2j+1)(\Omega_1^{(L)} + \ln g_L I)}. \quad (30)$$

As a result, the order-by-order cancellation of powers of  $\Omega_1$  arising from different layers, as established in [52], remains valid after the replacement

$\Omega_1^{(l)} \rightarrow \Omega_1^{(l)} + \ln g_l I$ . Due to the virtual noise scaling, the operator norm of  $\Omega_1^{(l)} + \ln g_l I$  is smaller than that of  $\Omega_1^{(l)}$ , which further enhances the effectiveness of the mitigation.

To experimentally demonstrate the applicability of VNS to dynamic circuits we revisit the four-qubit GHZ dynamic-circuit experiment carried out in [59]. Figure 4 shows how the fidelity curve improves when using VNS on the same experimental data. The method is also applicable to parity-based or reset-based SPAM mitigation introduced in [59]. In fact, this experiment already includes parity-based SPAM mitigation and parity based mid-circuit reset mitigation. VNS automatically address the SPAM noise as well. The measurement twirling applied in this experiment guarantees that the measurement noise is Hermitian.

#### IV. LAYER-BASED MITIGATION

In general, it is possible to divide the circuit into multiple layers, e.g., A and B, and mitigate each one separately such that

$$K_{mit,AB}^{(m)} = K_{mit,B}^{(m)} K_{mit,A}^{(m)}. \quad (31)$$

In the Appendix VI, we show that the runtime overhead in Taylor mitigation becomes

$$\mathcal{R} = \gamma_{tot}^2 \langle d \rangle = \gamma_m^2 \gamma_m^2 m. \quad (32)$$

At the same time, the infidelity becomes substantially smaller, since each layer experiences lower noise levels. For simplicity, we consider the case where the two layers have the same  $s_{min}$ , so that  $s_{min}^{tot} = s_{min}^2$ . The analysis can be extended to the case  $s_{min}^B \neq s_{min}^A$  by using a different mitigation order for each layer. Furthermore, we note that the layers can be chosen such that  $s_{min}^A \simeq s_{min}^B$ , for example by including the same number of two-qubit gates in each layer. In Appendix VI, we show that the unmitigated two-layer infidelity can be upper bounded by the individual layer infidelity

$$I_{op,tot}^{(0)} \leq I_{op,A}^{(0)} + I_{op,B}^{(0)} - I_{op,A}^{(0)} I_{op,B}^{(0)}, \quad (33)$$

and for the mitigated infidelity we get

$$I_{op,tot}^{(m)} \leq I_{op,A}^{(m)} + I_{op,B}^{(m)}. \quad (34)$$

The fact that this bound is less tight, since it does not include cross terms, is not critical because the mitigated infidelities are expected to be small, and the product correction is therefore negligible. Using  $s_{min}^{tot} = s_{min}^2$  we get

$$I_{op,AB}^{(m)} \leq 2I_{op}^{(m)}(\sqrt{s_{min}^{tot}}), \quad (35)$$

which is smaller than  $I_{op}^{(m)}(s_{min}^{tot})$  for any  $m$  and  $s_{min}$ . First we compare two-layer mitigation without VNS, as discussed above, with the standard single-layer Taylor mitigation (also without VNS). In the  $s_{min} = 0.4$  case studied in Fig. 2, the dashed orange curve shows that, despite the increased sampling overhead, two-layer mitigation is beneficial because the improvement in infidelity is larger. However, this is not true for all values of  $s_{min}$ .

Using the large- $m$  expansion, we find that the asymptotic (large- $m$ ) slopes of the  $\mathcal{R}$ -infidelity curves are

$$\frac{d \ln \mathcal{R}}{d \ln I_{op}}|_{Taylor-1L} = \frac{2 \ln 2}{\ln[1 - (s_{min}^{tot})^2]}, \quad (36)$$

$$\frac{d \ln \mathcal{R}}{d \ln I_{op}}|_{Taylor-2L} = \frac{4 \ln 2}{\ln(1 - s_{min}^{tot})}. \quad (37)$$

As shown in Fig. 5, a crossover occurs when these two slopes become equal at  $s_{min}^{tot} \simeq 0.62$ . Using the exact expressions for the infidelity and runtime overhead, we find that for finite order the crossover instead occurs at  $s_{min,2L}^{tot} \simeq 0.65$ . For  $s_{min}^{tot} \geq s_{min,2L}^{tot}$ , corresponding to weaker noise, single-layer mitigation is preferable. Below this value, two-layer mitigation is preferable. Note that for  $s_{min}^{tot} < s_{min,2L}^{tot}$ , part of the advantage comes from the fact that, for a given target infidelity, two-layer mitigation requires a lower mitigation order and therefore shorter circuits. However, the main contribution comes from the stronger reduction in infidelity.

For the two-layer case we use an upper bound on the infidelity rather than the exact infidelity. The exact infidelity depends on the specific circuit details, while the upper bound does not. As a result, in some cases the actual infidelity can be substantially smaller than the upper bound used here.

When further increasing the number of layers, we find an additional slope crossover between two-layer VNS and three-layer VNS at  $s_{min} \sim 0.5$ . However, when the advantage of three-layer VNS becomes significant, the required runtime overhead is substantial. For example, for  $I_{op}^{(0)} = 0.75$ , the sampling overhead is  $4.7 \times 10^8$  to achieve an infidelity of  $I_{op}^{(m=4)} = 0.014$ . Yet, this sampling overhead is 35 times smaller than that required for two-layer VNS.

Alternative multi-layer mitigation approaches have been studied in [60, 61]. However, these studies rely on different noise inversion schemes and are therefore outside the scope of the present analysis.

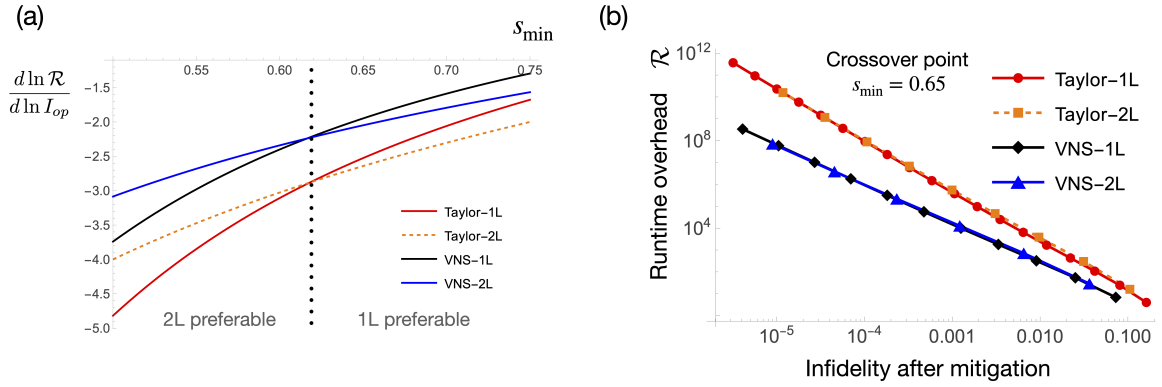


Figure 5. (a) Slopes of the  $\mathcal{R}$ -infidelity curves for various mitigation schemes as a function of the smallest eigenvalue of the noise operator,  $s_{\min}$ . Lower absolute values correspond to slower growth in mitigation overheads as infidelity decreases. Without VNS, two-layer Taylor mitigation outperforms single-layer mitigation when the noise is above a critical value ( $s_{\min}$  is below a critical value). The VNS slopes are always less steep (than the Taylor slopes, yet VNS also shows a crossover: beyond a critical noise value, two-layer VNS becomes more efficient than single-layer VNS in terms of runtime overhead. For both Taylor and VNS, the crossover value is  $\sim 0.62$  for  $m \rightarrow \infty$ , while for finite  $m$  we find the crossover to be  $\sim 0.65$ . (b) Same plot as Fig. 2(a) but at the crossover point  $s_{\min,2L}^{\text{tot}} = 0.65$ . While VNS still outperforms Taylor mitigation at this point, two-layer mitigation should be used only when the noise is stronger i.e.,  $s_{\min}^{\text{tot}} < s_{\min,2L}^{\text{tot}}$ .

## V. USING BOTH VIRTUAL NOISE SCALING AND LAYER-BASED MITIGATION

To further exploit the potential of the VNS approach, we next study the combination of two-layer mitigation and VNS. With VNS applied to each layer, and assuming as before that  $s_{\min}^A \simeq s_{\min}^B \simeq \sqrt{s_{\min}^{\text{tot}}}$ , the resulting infidelity is bounded by

$$I_{VNS-2L}^{(m)} \leq 2I_{op}^{(m)}[g_{eq}(\sqrt{s_{\min}^{\text{tot}}})\sqrt{s_{\min}^{\text{tot}}}], \quad (38)$$

and the two-layer runtime overhead  $\mathcal{R}$  is

$$\mathcal{R}_{VNS-2L} = \gamma^4(\sqrt{s_{\min}^{\text{tot}}})m. \quad (39)$$

The advantage of the two-layer VNS (VNS-2L) scheme is illustrated in Fig. 2 for  $s_{\min}^{\text{tot}} = 0.4$ . The blue curve shows that VNS-2L outperforms Taylor-1L, Taylor-2L, and VNS-1L. As in the no-VNS case discussed in the previous section, we observe a crossover between VNS-2L and VNS-1L. VNS-2L has lower runtime overhead compared to VNS-1L when  $s_{\min}^{\text{tot}} \leq s_{\min,2L} \simeq 0.65$ . Figure 5 shows the crossover in the large  $m$  limit.

As shown in Fig. 2, for a mitigated infidelity of 0.024 (right vertical line), we find a reduction of  $\mathcal{R}$  from  $3.6 \times 10^8$  in the Taylor-1L method to  $3.8 \times 10^4$  in the VNS-2L method. For lower mitigated infidelity, the advantage is even larger. If the mitigated infidelity is  $9 \times 10^{-3}$ , we obtain a reduction of  $\mathcal{R}$  from  $3.6 \times 10^{11}$  in the Taylor-1L method to  $9.4 \times 10^5$  in the VNS-2L method. This corresponds to a reduction of  $\mathcal{R}$  by a factor of  $10^4$  in the first case and  $10^5$  in the second case. The asymptotic slopes ( $m \gg 1$ ) in the VNS case are

$$\frac{d \ln \mathcal{R}}{d \ln I_{op}}|_{VNS-1L} = \frac{2 \ln \left( \frac{2}{(s_{\min}^{\text{tot}})^2 + 1} + 1 \right)}{\ln \left( \frac{2}{(s_{\min}^{\text{tot}})^2 + 1} - 1 \right)}, \quad (40)$$

$$\frac{d \ln \mathcal{R}}{d \ln I_{op}}|_{VNS-2L} = \frac{2 \ln \left( \frac{2}{s_{\min}^{\text{tot}} + 1} + 1 \right)}{\ln \left( \frac{2}{s_{\min}^{\text{tot}} + 1} - 1 \right)}. \quad (41)$$

Equations (35) - (41) together with Figs. 2 and 5 constitute our main findings: orders of magnitude reduction compared to the baseline one-layer Taylor mitigation (Richardson extrapolation).

## VI. CONCLUDING REMARKS

The analysis based on the VNS scaling factor  $g = \sqrt{2/(1 + s_{\min}^2)}$  is agnostic to the target observable, initial condition, circuit size, noise type, and circuit topology. As a result, the conclusions are broadly applicable. Regarding the noise model, we assume that the native noise is Hermitian and discuss how arbitrary Markovian noise can be brought into this form. The results presented here correspond to the worst-case scenario. In non-worst-case situations, VNS may provide little or no benefit. However, this is not due to a limitation of VNS, but rather to the exceptionally strong performance of Taylor mitigation as a starting point. Thus, even in such cases, the observable error remains bounded by the worst-case VNS error limits derived in this work.

While  $s_{\min}^2$  (or more precisely, a lower bound on it) can be estimated from known gate errors, we also introduce a method that accounts for the initial condition and the target observable. In this approach, the VNS parameter  $g$  is determined by analyzing the extrema and inflection points of the mitigated expectation value as a function of  $g$ . This can significantly reduce the runtime overhead compared to the worst-case estimate.

VNS is compatible with dynamic circuit measurements and inherits the drift-resilience and bias-free properties of the Layered-KIK method [52]. It can also be used to improve the performance of noise-amplification-based measurement error mitigation [59].

The relative reduction in the runtime overhead required to reach a target infidelity is substantial in the strong-noise regime. However, this improvement may not be immediately visible on current devices, since the most pronounced gains occur when the baseline runtime overhead without VNS is already extremely large. For example, improvements of  $10^4$  and  $10^5$  were observed for baseline overheads of  $10^8$  and  $10^{11}$ , respectively. Even after these improvements, the remaining runtime overhead is still significant. Consequently, in addition to standard sequential execution, massive parallel execution of shots is required across different qubit sets, quantum cores, and even multiple quantum computers. VNS transforms previously inconceivable overheads into challenging but realistic targets, especially as large-scale production of NISQ and fault-tolerant devices becomes feasible.

## ACKNOWLEDGMENTS

Raam Uzdin is grateful for support from the Israel Science Foundation (Grants No. 2724/24). The support of the Israel Innovation Authority is greatly appreciated.

---

[1] Y. Suzuki, S. Endo, K. Fujii, and Y. Tokunaga, *PRX Quantum* **3**, 010345 (2022).

[2] C. Piveteau, D. Sutter, S. Bravyi, J. M. Gambetta, and K. Temme, *Physical review letters* **127**, 200505 (2021).

[3] M. Lostaglio and A. Ciani, *Physical review letters* **127**, 200506 (2021).

[4] D. Aharonov, O. Alberton, I. Arad, Y. Atia, E. Bairey, Z. Brakerski, I. Cohen, O. Golan, I. Gurwich, O. Kenneth, *et al.*, arXiv preprint arXiv:2503.17243 (2025).

[5] M. A. Wahl, A. Mari, N. Shammah, W. J. Zeng, and G. S. Ravi, in *2023 IEEE International Conference on Quantum Computing and Engineering (QCE)*, Vol. 1 (IEEE, 2023) pp. 888–897.

[6] D. Aharonov, Y. Atia, E. Bairey, Z. Brakerski, I. Cohen, O. Golan, I. Gurwich, N. H. Lindner, and M. Shutman, arXiv preprint arXiv:2512.23810 (2025).

[7] Z. Zhou, S. Pexton, A. Kubica, and Y. Ding, arXiv preprint arXiv:2512.09863 (2025).

[8] Z. Cai, R. Babbush, S. C. Benjamin, S. Endo, W. J. Huggins, Y. Li, J. R. McClean, and T. E. O’Brien, arXiv preprint arXiv:2210.00921 (2022).

[9] D. Qin, X. Xu, and Y. Li, *Chinese Physics B* **31**, 090306 (2022).

[10] S. Endo, Z. Cai, S. C. Benjamin, and X. Yuan, *Journal of the Physical Society of Japan* **90**, 032001 (2021).

[11] K. Temme, S. Bravyi, and J. M. Gambetta, *Physical review letters* **119**, 180509 (2017).

[12] Y. Quek, D. Stilck França, S. Khatri, J. J. Meyer, and J. Eisert, *Nature Physics* **20**, 1648 (2024).

[13] R. Takagi, S. Endo, S. Minagawa, and M. Gu, *npj Quantum Information* **8**, 114 (2022).

[14] Y. Li and S. C. Benjamin, *Physical Review X* **7**, 021050 (2017).

[15] S. Endo, S. C. Benjamin, and Y. Li, *Physical Review X* **8**, 031027 (2018).

[16] A. Strikis, D. Qin, Y. Chen, S. C. Benjamin, and Y. Li, *PRX Quantum* **2**, 040330 (2021).

[17] P. Czarnik, A. Arrasmith, P. J. Coles, and L. Cincio, *Quantum* **5**, 592 (2021).

[18] B. Koczor, *Physical Review X* **11**, 031057 (2021).

[19] W. J. Huggins, S. McArdle, T. E. O’Brien, J. Lee, N. C. Rubin, S. Boixo, K. B. Whaley, R. Babbush, and J. R. McClean, *Physical Review X* **11**, 041036 (2021).

[20] T. Giurgica-Tiron, Y. Hindy, R. LaRose, A. Mari, and W. J. Zeng, in *2020 IEEE International Conference on Quantum Computing and Engineering (QCE)* (IEEE, 2020) pp. 306–316.

- [21] Z. Cai, *Quantum* **5**, 548 (2021).
- [22] A. Mari, N. Shammah, and W. J. Zeng, *Physical Review A* **104**, 052607 (2021).
- [23] M. Huo and Y. Li, *Physical Review A* **105**, 022427 (2022).
- [24] A. Lowe, M. H. Gordon, P. Czarnik, A. Arrasmith, P. J. Coles, and L. Cincio, *Physical Review Research* **3**, 033098 (2021).
- [25] P. D. Nation, H. Kang, N. Sundaresan, and J. M. Gambetta, *PRX Quantum* **2**, 040326 (2021).
- [26] H. Liao, D. S. Wang, I. Siddikov, C. Salcedo, A. Seif, and Z. K. Minev, *Nature Machine Intelligence* , 1 (2024).
- [27] S. Bravyi, S. Sheldon, A. Kandala, D. C. McKay, and J. M. Gambetta, *Physical Review A* **103**, 042605 (2021).
- [28] Y. Kim, C. Wood, T. Yoder, S. Merkel, J. Gambetta, K. Temme, and A. Kandala, *arXiv preprint arXiv:2108.09197* (2021).
- [29] E. Berg, Z. Minev, A. Kandala, and K. Temme, *arXiv preprint arXiv:2201.09866* (2022).
- [30] A. Kandala, K. Temme, A. D. Corcoles, A. Mezzacapo, J. M. Chow, and J. M. Gambetta, *Nature* **567**, 491 (2019).
- [31] C. Song, J. Cui, H. Wang, J. Hao, H. Feng, and Y. Li, *Science advances* **5**, eaaw5686 (2019).
- [32] F. Arute, K. Arya, R. Babbush, and et al., *Science* **369**, 1084 (2020).
- [33] M. Urbanek, B. Nachman, V. R. Pascuzzi, A. He, C. W. Bauer, and W. A. de Jong, *Physical Review Letters* **127**, 270502 (2021).
- [34] S. Zhang, Y. Lu, K. Zhang, W. Chen, Y. Li, J.-N. Zhang, and K. Kim, *Nature communications* **11**, 1 (2020).
- [35] R. Sagastizabal, X. Bonet-Monroig, M. Singh, M. A. Rol, C. Bultink, and et al., *Physical Review A* **100**, 010302 (2019).
- [36] A. He, B. Nachman, W. A. de Jong, and C. W. Bauer, *Physical Review A* **102**, 012426 (2020).
- [37] S. Filippov, M. Leahy, M. A. Rossi, and G. García-Pérez, *arXiv preprint arXiv:2307.11740* (2023).
- [38] C. Kim, K. D. Park, and J.-K. Rhee, *IEEE Access* **8**, 188853 (2020).
- [39] S. Cantori, A. Mari, D. Vitali, and S. Pilati, *EPJ Quantum Technology* **11**, 1 (2024).
- [40] T. Araki, J. F. Goodwin, and B. Koczor, *arXiv preprint arXiv:2503.19245* (2025).
- [41] B. Bakó, T. Araki, and B. Koczor, *arXiv preprint arXiv:2506.04380* (2025).
- [42] R. Haghshenas, E. Chertkov, M. Mills, W. Kadow, S.-H. Lin, Y.-H. Chen, C. Cade, I. Niesen, T. Begušić, M. S. Rudolph, et al., *arXiv preprint arXiv:2503.20870* (2025).
- [43] Y. Kim, A. Eddins, S. Anand, K. X. Wei, E. Van Den Berg, S. Rosenblatt, H. Nayfeh, Y. Wu, M. Zaletel, K. Temme, et al., *Nature* **618**, 500 (2023).
- [44] Y. Kim, L. C. Govia, A. Dane, E. v. d. Berg, D. M. Zajac, B. Mitchell, Y. Liu, K. Balakrishnan, G. Keefe, A. Stabile, et al., *arXiv preprint arXiv:2407.02467* (2024).
- [45] S. Dasgupta, T. S. Humble, and A. Danageozian, in *2023 IEEE International Conference on Quantum Computing and Engineering (QCE)*, Vol. 1 (IEEE, 2023) pp. 99–110.
- [46] B. Koczor, *Physical Review X* **11**, 031057 (2021).
- [47] Y. Kim, C. J. Wood, T. J. Yoder, S. T. Merkel, J. M. Gambetta, K. Temme, and A. Kandala, *Nature Physics* , 1 (2023).
- [48] R. Majumdar, P. Rivero, F. Metz, A. Hasan, and D. S. Wang, in *2023 IEEE International Conference on Quantum Computing and Engineering (QCE)*, Vol. 1 (IEEE, 2023) pp. 881–887.
- [49] V. R. Pascuzzi, A. He, C. W. Bauer, W. A. de Jong, and B. Nachman, *Phys. Rev. A* **105**, 042406 (2022).
- [50] A. He, B. Nachman, W. A. de Jong, and C. W. Bauer, *Phys. Rev. A* **102**, 012426 (2020).
- [51] I. Henao, J. P. Santos, and R. Uzdin, *npj Quantum Information* **9**, 120 (2023).
- [52] B. Bar, J. P. Santos, and R. Uzdin, *arXiv preprint arXiv:2504.12457* (2025).
- [53] E. Knill, *arXiv preprint quant-ph/0404104* (2004).
- [54] R. Harper, S. T. Flammia, and J. J. Wallman, *Nature Physics* **16**, 1184 (2020).
- [55] Z. Cai and S. C. Benjamin, *Scientific reports* **9**, 11281 (2019).
- [56] J. P. Santos, B. Bar, and R. Uzdin, *npj Quantum Information* **10**, 100 (2024).
- [57] J. A. Gyamfi, *European Journal of Physics* **41**, 063002 (2020).
- [58] D. Aharonov, O. Alberton, I. Arad, Y. Atia, E. Bairey, M. B. Dov, A. Berkovitch, Z. Brakerski, I. Cohen, E. Fuchs, et al., *arXiv preprint arXiv:2508.10997* (2025).
- [59] J. P. Santos and R. Uzdin, *arXiv preprint arXiv:2506.11270* (2025).
- [60] V. Russo and A. Mari, *Phys. Rev. A* **110**, 062420 (2024).
- [61] Y.-H. Chen, *arXiv preprint arXiv:2506.04468* (2025).

## APPENDIX I - EFFECTIVE HERMITICITY OF THE NOISE

In general, the noise in the circuit is not Hermitian, even if the native Lindbladian noise generators  $\mathcal{L}(t)$  are Hermitian. Using the Magnus expansion in the interaction picture in Liouville space, the noise channel of the full circuit is

$$N = e^{\Omega_1 + \Omega_2 + O(\Omega_3)}, \quad (42)$$

where

$$\Omega_1 = \int_0^t \mathcal{L}^{int}(t') dt', \quad (43)$$

$$\Omega_2 = \frac{1}{2} \left[ \int_0^t \int_0^{t'} dt dt' [\mathcal{L}^{int}(t'), \mathcal{L}^{int}(t'')] \right], \quad (44)$$

and

$$\mathcal{L}^{int}(t) = \mathcal{U}^\dagger(t) \mathcal{L}(t) \mathcal{U}(t). \quad (45)$$

Next, we assume the native noise is either inherently Hermitian or is rendered Hermitian by pseudo-twirling in sufficiently small layers. If  $\mathcal{L}^\dagger(t) = \mathcal{L}(t)$  then  $\Omega_1 = \Omega_1^\dagger$ ,  $\Omega_2 = -\Omega_2^\dagger$  and  $\Omega_3 = \Omega_3^\dagger$ . Thus, the leading-order correction to Hermiticity is  $\Omega_2$ . In [52], it was shown that amplification by layers (not to be confused with mitigation by layers in the current paper) leads to strong suppression of  $\Omega_2$ . When the layers are sufficiently thin, this suppression scales as  $1/N_{\text{layers}}^2$ , where  $N_{\text{layers}}$  is the chosen number of layers. Note that the layers are not necessarily related to gates or groups of gates; a single gate can be sliced into multiple layers. When the layers are not sufficiently thin, there is a bound showing that the  $\Omega_2$  contribution decreases as  $1/N_{\text{layers}}$ .

The  $\Omega_2$  contribution is typically much smaller than  $\Omega_1$  when the noise is *benign* (see definition in the main text). Therefore, dozen layers often make the effective  $\Omega_2$  contribution negligible. In this case, the effective noise channel is

$$N_{\text{eff}} = N_{\text{eff}}^\dagger + O(\Omega_2^3, \Omega_4). \quad (46)$$

Note that  $\Omega_2^2$  is Hermitian when  $\mathcal{L}^\dagger(t) = \mathcal{L}(t)$ , so potential corrections arise only from  $\Omega_2^3$ . We conclude that when using the Taylor coefficients (or the scaled Taylor coefficients studied in this work) together with amplification in layers, the effective noise circuit is Hermitian for all practical purposes if  $\mathcal{L}^\dagger(t) = \mathcal{L}(t)$ .

## APPENDIX II - AVERAGE CIRCUIT DEPTH

For a single layer, we optimize the shot allocation such that, for a fixed total number of shots  $N_{\text{tot}} = \sum N_i$ , the variance  $\sum_i \frac{a_i^2}{N_i}$  is minimized. This minimization yields  $\sum_i \frac{a_i^2}{N_i} = \frac{1}{N_{\text{tot}}} (\sum_i |a_i|)^2$ . This result can be obtained using a Lagrange multiplier. Setting the partial derivatives to zero we get

$$\frac{d}{dN_i} \left( \sum_{i=0}^m \frac{a_i^2}{N_i} + \lambda (\sum_{i=0}^m N_i - N_{\text{tot}}) \right) = -\frac{a_i^2}{N_i^2} + \lambda = 0, \quad (47)$$

we find

$$N_i = |a_i| / \lambda, \quad (48)$$

$$\sum_{i=0}^m N_i = \sum_{i=0}^m |a_i| / \lambda, \quad (49)$$

$$N_{\text{tot}} = \gamma / \lambda, \quad (50)$$

$$a_i^2 / N_i = |a_i| \lambda = |a_i| \gamma / N_{\text{tot}}, \quad (51)$$

Where  $\gamma \doteq \sum_{i=0}^M |a_i|$ . As a result, the variance of the average over  $N_{\text{tot}}$  shots is

$$\sum_{i=0}^m \frac{a_i^2}{N_i} = \gamma^2 / N_{\text{tot}}. \quad (52)$$

Next, we assume that  $N_{\text{tot}}$  already includes the sampling overhead  $\gamma^2$ , and we calculate the total runtime while accounting for the fact that different noise-amplified circuits have different depths. We find

$$N_{\text{tot}} \sum_{i=0}^m \frac{N_i}{N_{\text{tot}}} (2i + 1) = N_{\text{tot}} \sum_{i=0}^m \frac{|a_i| / \lambda}{N_{\text{tot}}} (2i + 1) = N_{\text{tot}} \sum_{i=0}^m \frac{|a_i| N_{\text{tot}} / \gamma}{N_{\text{tot}}} (2i + 1) = N_{\text{tot}} \sum_{i=0}^m \frac{|a_i|}{\gamma} (2i + 1). \quad (53)$$

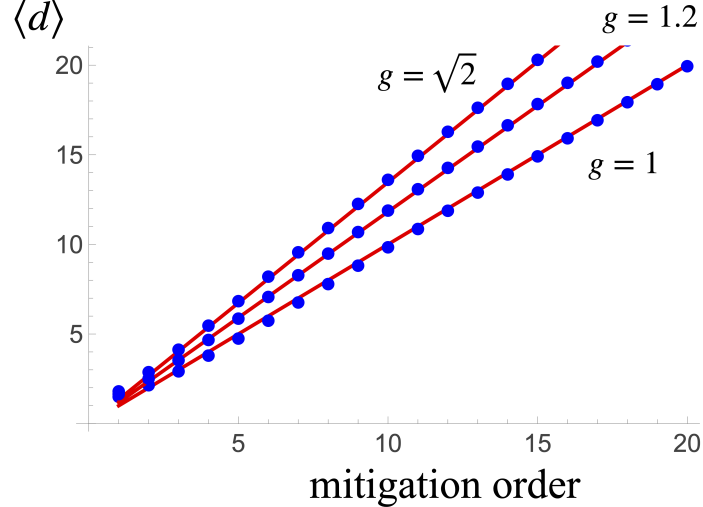


Figure 6. Average circuit depth  $\langle d \rangle$  as a function of the mitigation order  $m$  for different values of the VNS parameter  $g$ . Markers show the numerical values, while the lines represent the approximation  $\langle d \rangle \simeq (1 + \ln g)m$ .

Hence, the average circuit depth is

$$\langle d \rangle = \sum_{i=0}^m \frac{|a_i|}{\gamma} (2i + 1). \quad (54)$$

The runtime overhead is given by the time required to run  $N_{tot}$  shots with the averaged increased circuit depth, divided by the time required to run  $N$  shots of the unamplified circuit with the same accuracy. Using  $N_{tot} = \gamma^2 N$ , we obtain that the runtime overhead is

$$\mathcal{R} = \gamma^2 \langle d \rangle. \quad (55)$$

As shown in Fig. 6,  $\langle d \rangle$  is predominantly linear in the mitigation order  $m$ . In particular we find that

$$\langle d \rangle = \sum_{i=0}^m \frac{|a_i(g)|}{\gamma} (2i + 1) \cong (1 + \ln g)m. \quad (56)$$

### Two-layer case

Assuming the first layer occupies a fraction  $\alpha$  of the total circuit length, we obtain

$$\begin{aligned} \langle d \rangle &= \sum_{i,j=0}^m \frac{|a_i|}{\gamma} \frac{|a_j|}{\gamma} [\alpha(2i + 1) + (1 - \alpha)(2j + 1)] = \sum_{i,j=0}^m \frac{|a_i|}{\gamma} \frac{|a_j|}{\gamma} (2i + 1)\alpha + \sum_{i,j=0}^m \frac{|a_i|}{\gamma} \frac{|a_j|}{\gamma} (2j + 1)(1 - \alpha) \\ &= \sum_{i,j=0}^m \frac{|a_i|}{\gamma} (2i + 1) = (1 + \ln g)m, \end{aligned} \quad (57)$$

where we have used approximation in Eq. (56).

### APPENDIX III - ANALYTICAL CHOICE OF THE VNS PARAMETER

We start with the large  $m$  approximation for the infidelity

$$I_{op}^{(m \gg 1)}(s_{\min}) \simeq \frac{(1 - s_{\min}^2)^{m+1}}{\sqrt{\pi m s_{\min}}}. \quad (58)$$

Next, to obtain comparable errors at both ends of the scaled noise interval  $[gs_{\min}, g]$ , we impose the condition:

$$I_{op}^{(m \gg 1)}(gs_{\min}) = I_{op}^{(m \gg 1)}(g). \quad (59)$$

This simplifies to

$$\frac{(1 - g^2 s_{\min}^2)^{m+1}}{s_{\min}} = (g^2 - 1)^{m+1}, \quad (60)$$

and finally yields

$$\bar{g} = \sqrt{\frac{1 + s_{\min}^{\frac{1}{m+1}}}{s_{\min}^2 + s_{\min}^{\frac{1}{m+1}}}}. \quad (61)$$

Since  $0 < s_{\min} \leq 1$ , we get that

$$\bar{g} = \sqrt{\frac{1 + s_{\min}^{\frac{1}{m+1}}}{s_{\min}^2 + s_{\min}^{\frac{1}{m+1}}}} \geq \sqrt{\frac{2}{s_{\min}^2 + 1}} = g_{eq}. \quad (62)$$

We have not observed a significant advantage in using  $\bar{g}$  instead of  $g_{eq}$ . For low orders,  $\bar{g}$  slightly overestimates the  $g_{exact}$  value for which  $I_{op}(g_{exact} s_{\min}) = I_{op}(g_{exact})$ . Hence, the actual infidelity value is  $\max(I_{op}(\bar{g} s_{\min}), I_{op}(\bar{g})) = I_{op}(\bar{g})$ . In contrast,  $g_{eq}$  slightly underestimate  $g_{exact}$ , and therefore  $\max(I_{op}(g_{eq} s_{\min}), I_{op}(g_{eq})) = I_{op}(g_{eq} s_{\min})$ . Note that  $g_{eq}$  can be obtained directly from Eq. (60) by setting  $s_{\min} = 1$  in the denominator of the expression in the left-hand side. Alternatively, it holds that  $g_{eq} = \lim_{m \rightarrow \infty} \bar{g}$ .

#### APPENDIX IV - RELATING INFIDELITIES OF LAYERS TO CIRCUIT INFIDELITY

We start by relating the smallest singular value of the whole circuit to that of the layers in the absence of mitigation. For simplicity we consider two layers

$$K_{AB} = U_B N_B U_A N_A \doteq U_B U_A \tilde{N}_B N_A. \quad (63)$$

Since the infidelity is determined by  $I_{op}^{(m)}(s_{\min})$  we focus first on the smallest singular value  $s_{\min}$

$$s_{\min} = \frac{1}{\|N^{-1}\|_{(op)}}, \quad (64)$$

and therefore

$$s_{\min}(K_{AB}) = \frac{1}{\|(\tilde{N}_B N_A)^{-1}\|} = \frac{1}{\|N_A^{-1} \tilde{N}_B^{-1}\|} \geq \frac{1}{\|N_A^{-1}\|} \frac{1}{\|N_B^{-1}\|} = s_{\min}(K_A) s_{\min}(K_B), \quad (65)$$

where we have used unitary invariance and submultiplicativity of the operator norm. From this one concludes that for multiple layers the total  $s_{\min}$  can be estimated by knowing the noise of the layers (or the individual gates). The estimate will overestimate the error due to the inequalities used in the derivation. More generally we can write:

$$s_{\min}(K^{tot}) \geq \prod_l s_{\min,l}. \quad (66)$$

First we address the infidelity of the unmitigated circuits  $I_{op}^{(0)} = 1 - s_{\min}$  (for Hermitian noise). Using the definition of  $I_{op}^{(0)}$  in (66) leads to

$$I_{op,tot}^{(0)} = 1 - s_{\min}^{tot} \leq 1 - \prod_l (1 - I_{op,l}^{(0)}). \quad (67)$$

This relation sets an upper bound on the infidelity of the whole circuit in terms of the layers infidelities. This bound is more refined than simply summing the infidelities. Yet, at the same time, it is still a simple function of the layer infidelities. For example, in two layers we have

$$I_{op,tot}^{(0)} \leq I_{op,A}^{(0)} + I_{op,B}^{(0)} - I_{op,A}^{(0)} I_{op,B}^{(0)}. \quad (68)$$

Next, we want to treat the total infidelity in mitigation of two layers where each layer is potentially mitigated to a different order:

$$K_{mit,tot}^{(m_A, m_B)} = K_{mit,B}^{(m_B)} K_{mit,A}^{(m_A)}. \quad (69)$$

The infidelity for Hermitian noise is

$$\begin{aligned} & \left\| U_B U_A - K_{mit,tot}^{(m_A, m_B)} \right\| = \\ & \left\| I - U_A^\dagger [I - (I - \sum_{s_B} f_{m_B}(s_B) |s_B\rangle \langle s_B|) U_A [I - (I - \sum_{s_A} f_{m_A}(s_A) |s_A\rangle \langle s_A|)]] \right\| = \\ & \left\| U_A^\dagger (I - \sum_{s_B} f_{m_B}(s_B) |s_B\rangle \langle s_B|) U_A + (I - \sum_{s_A} f_{m_A}(s_A) |s_A\rangle \langle s_A|) - \right. \\ & \left. U_A^\dagger (I - \sum_{s_B} f_{m_B}(s_B) |s_B\rangle \langle s_B|) U_A (I - \sum_{s_A} f_{m_A}(s_A) |s_A\rangle \langle s_A|) \right\|. \end{aligned} \quad (70)$$

By using the triangle inequality and submultiplicativity for the last term we get

$$\left\| U_B U_A - K_{mit,tot}^{(m_A, m_B)} \right\| \leq I_{op}^{(m_A)}(s_{\min,A}) + I_{op}^{(m_B)}(s_{\min,B}) + I_{op}^{(m_A)}(s_{\min,A}) I_{op}^{(m_B)}(s_{\min,B}). \quad (72)$$

While for  $m_A = m_B = 0$  the bound (68) is tighter than this bound, the current bound is applicable to any  $m_A, m_B$ . Moreover, when  $m_A$  and  $m_B$  are sufficiently large  $I_{op}^{(m_A)}(s_{\min,A}) + I_{op}^{(m_B)}(s_{\min,B}) \gg I_{op}^{(m_A)}(s_{\min,A}) I_{op}^{(m_B)}(s_{\min,B})$  and the product term in (72) can be neglected.